ARCHIVE OF MECHANICAL ENGINEERING

DOI: 10.24425/ame.2023.145581 2023, Vol. 70, No. 2, pp. 219–245

Rahul GAJI [1,2], Ashish DOSHI [2], Mukund BADE [2],
Punit SINGH[3]

Influence of impeller blade rounding and surface roughness on the internal hydraulics and performance of pump as turbine

Received 28 November 2022, **Revised** 13 February 2023, **Accepted** 28 February 2023, **Published online** 11 April 2023

Keywords: pump as turbine, impeller blade rounding, CFD analysis of PAT, simple modifications in PAT, hydraulic analysis

The Pump As Turbine (PAT) is an important technology for low-cost micro-hydropower and energy recovery, and hence the internal hydraulics of PAT needs to be clearly understood. Additionally, during its operation, the sediments in the water increase the roughness of the internal surfaces and may alter the internal hydraulics and PAT performance similar to a centrifugal pump or Francis turbine. The researchers tried hard to perform simple modifications such as impeller blade rounding to increase the efficiency of PAT. In this paper, the developed test rig is used to analyze the performance of the impeller blade rounding and is validated with a numerical model. This numerical model is further used to study the influence of impeller blade rounding and surface roughness on internal hydraulics and PAT performance. The impeller blade rounding at the most increased the PAT efficiency by 1–1.5% at the Best efficiency point (Q=16.8 lps), mainly due to the wake reduction on the suction side and increased flow area. With increasing the surface roughness from 0–70 µm, the PAT efficiency is decreased maximum by 4%. The efficiency was mainly reduced due to increased hydraulic losses at flow zone and disk friction losses at the non-flow zone.

✉ Mukund BADE, e-mail: bmh@med.svnit.ac.in

[1] Annasaheb Dange College of Engineering and Technology, Ashta, India; ORCID: 0000-0002-8083-5125

[2] Sardar Vallabhbhai National Institute of Technology, Surat, Gujarat, India; ORCIDs: A.D. 0000-0002-4107-7464; M.B. 0000-0002-7790-2710

[3] Centre for Sustainable Technologies, Indian Institute of Science, Bangalore, India

Nomenclature

C	absolute velocity, m/s
g	gravitational acceleration, m/s^2
u	tangential blade velocity, m/s
c_f	friction factor
f_R	roughness factor
f_L	leakage flow factor
H	net head, m
h	head, m
k_o	rotation factor
k_{RR}	disk friction factor
P_{RR}	disk friction power per side of a disk, W
P	power, W
Q	discharge, lps
r	radius, m
Re	Reynolds number
T	torque, Nm

Greek symbol

Δ	difference
ε	surface roughness, µm
η	efficiency, %
ρ	mass density, kg/m^3
ω	angular velocity, rad/s

Abbreviations

BEP	Best Efficiency Point
CFD	Computational Fluid Dynamics
FZ	Flow zone
NFZ	Non-flow zone
PAT	Pump As Turbine
rpm	revolution per minute

Subscripts

1	impeller inlet (turbine mode)
2	impeller outlet (turbine mode)
imp	impeller
L	losses
out	outlet
u	tangential component
vol	volute

1. Introduction

Micro-hydropower plants are generally considered green energy sources due to their socio-ecological balance. These plants can be grid-connected as well as off-grid power generation units. The standalone off-grid hydropower stations are cost-effective solutions for remote locations, rural areas, and isolated communities.

It reduces the transmission losses of long-distance transmission lines and capital costs [1]. For such plants, the cost share of electromechanical equipment (mainly turbine) is dominating in the total project cost [2]. Therefore, the conventional water turbine installation for the micro-hydropower plant is not economically feasible [3]. Pump as turbine (PAT) is one of the most sustainable, cheaper, and proven alternative solutions for such plants [4]. Nowadays, along with the standalone power station, PAT finds applications as small pumped storage power plants, reverse osmosis systems, energy recovery systems such as water distribution networks, irrigation, and sewage system for replacement of pressure-reducing valves, etc. However, one of the critical challenges is its lower performance than conventional turbines as it is not designed as a turbine [5]. Therefore, continuous attempts to improve the PAT's performance are an ongoing process.

Many researchers have proposed low-cost, simple modifications for the impeller and volute (geometrical modifications) to increase the performance of PAT, keeping cost benefits intact. One such simple modification involves rounding of the impeller blades and shrouds [5–9], which altogether may contribute 1 to 1.5% enhancements in the PAT performance. Some researchers proposed a method of back cavity filling with solid material of appropriate size and shape to reduce the disk friction loss and to increase the PAT efficiency [10]. Another modification proposed is the addition of the splitter blades to the impeller inlet, investigated through CFD-based numerical simulation [4, 11]. It revealed that at the Best Efficiency Point (BEP) and overload region, the PAT efficiency is enhanced by 2.7 to 3.42% due to the reduction of vortices and blade separation. There are other simple modifications, but they are not always beneficial. Generally, the main objectives of the simple modifications are to minimize the various losses associated with PAT in the flow zone or in the non-flow zone and increase the PAT performance without altering the cost benefit of it [5, 12].

To understand internal flow hydraulics in the PAT, many researchers proposed the CFD as an important tool. Derakhshan and Kasaeian [13] proposed CFD as a design tool for a propeller pump and applied it in forward and reverse operations. Yang et al. [14] performed an analysis based on Ansys-CFX to understand the internal parameters variation such as radial gaps for steady flow simulation. CFD and ANN-based methodology is developed to optimize the blade section of the impeller to improve the PAT efficiency [15]. The internal flow physics, mainly the separation of fluid flow, is analyzed at the impeller through numerical simulation using CFX [16]. The CFD tool is proven to understand the internal flow physics of PAT. Though many authors have incorporated impeller blade rounding (IBR) modification and experimentally showed 1–1.5% enhancement in the performance [6], the internal flow physics contributed to the performance enhancement is not yet understood at different loading conditions and thereby it is not clear the scope and means for further improvement. Therefore, a detailed CFD-based numerical investigation is essential to analyze the influence of IBR on the performance and flow physics in flow control volumes of PAT.

Along with the performance improvement of PAT by various means, it is also necessary to study parameters that can influence PAT's performance during its operation. It is generally observed that water used to run the PAT contains impurities such as silt and solid particles affecting the surface roughness of the impeller and internal surfaces of the volute. These water impurities adversely affect the performance of PAT due to an increase in surface roughness (ε). Therefore, ε is one of the critical parameters influencing PAT performance, which needs to be studied in detail [17, 18]. Further, it is noticed that the studies on the effect of ε in the case of PAT are hardly available in the open literature. As the working of PAT is related to the Francis turbine, the literature on the effect of ε on the Francis turbine is reviewed in the following paragraph.

The installation of hydro turbines on sediment-laden rivers especially in the Asian mountains range is the biggest challenge due to the erosion of turbines from the abrasive action of quartz and feldspar [19]. In addition, slurry erosion in the Francis turbine is one of the critical problems, especially during the rainy season, due to the increase in the number of solid particles impacting the surfaces, particularly in systems where an exhaustive filtration process is impossible [20, 21]. These silt and contaminants in the water change the ε of the turbine components, especially turbine blades, and volute [22]. PAT may be subjected to similar effects due to impurities and silt, which increases the ε of volute and impeller.

The present work aims to perform the experiment on the developed PAT test rig for without IBR and with IBR stages. These experimental results are used to validate the numerical model developed using CFD software. Afterward, the validated numerical model is used to investigate the effect of IBR on the efficiency and internal flow physics of PAT and to find the further scope of performance improvement. Additionally, the influence of surface roughness on the PAT efficiency is analyzed with the help of flow physics. This effect is analyzed at BEP for three different configurations, viz. (i) uniformly varying the surface roughness of all the components for without IBR and with IBR; (ii) varying the surface roughness at volute and constant at the impeller for without IBR, and (iii) varying the surface roughness at the impeller and constant at volute for without IBR stage. Overall, in this work, with the help of state-of-the-art test facility of PAT, the developed numerical model is validated and then the same model is used to analyze the internal flow physics and surface roughness analysis for various configurations of PAT.

2. Experimental set up

The state-of-the-art test facility is developed with sophisticated measuring instruments to understand the influence of IBR on the performance of PAT [12] and validate the numerical model developed through CFD software. The schematic of the experimental setup is shown in Fig. 1. The PAT test rig consists of a feed pump, end suction centrifugal pump to be tested in turbine mode operation attached with the eddy current dynamometer and draft tube, and piping system.

The magnetic flow meter, pressure transmitter, speed sensor, and torque sensor are installed to measure the flow rate, pressure, speed, and torque respectively. The variable frequency drive is used to maintain the speed. The test rig is supported with SCADA software-based programmable logic controller for automatic control and data logging system during operation. The detailed specification of measuring instruments is given in Table A1 (refer Appendix A.1). The low specific speed 19.9 rpm [discharge based pump mode specific speed, $N_{qp} = NQ^{1/2}/H^{3/4}$ (m, m^3/s)] end suction centrifugal pump is selected for turbine mode operation. At BEP, the selected pump delivers 17.5 lps flow rate at 20.4 m head when operated at 1450 rpm. Table 1 illustrates the main geometric parameters of the impeller. It is important to note that this state-of-the-art facility shows excellent repeatability and quite a lower value of uncertainty as presented in Table A2 of Appendix A.1 (repeatability is presented in Fig. A.1 of Appendix A.1), which is within the limit to justify the results. The fluid from volute enters to the impeller inlet where it strikes on the sharp bladed impeller which adversely affects the flow behavior and PAT performance [6]. This sharp edge of the impeller blade at the inlet is rounded as shown in Fig. 2 with a radius equal to half the thickness of the blade (refer Fig. A2 in Appendix A.2 for impeller inlet and outlet diameters presentation). The experiments are performed for without IBR and with IBR stages of PAT. The results are generated in the form of characteristic curves at a constant speed.

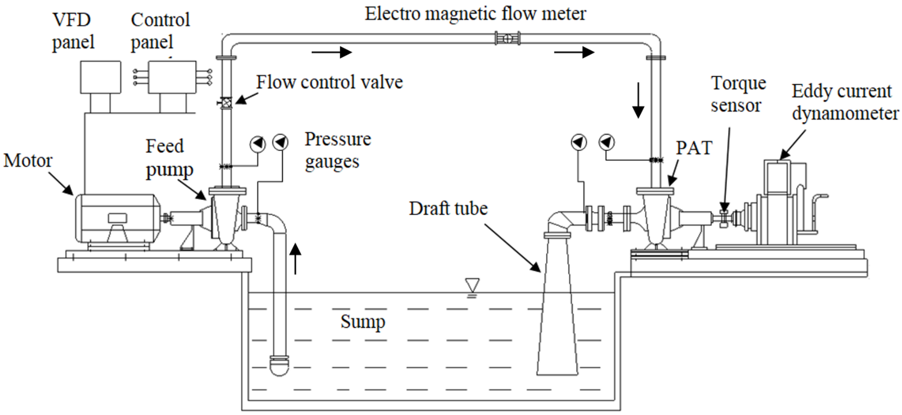

Fig. 1. Schematic of PAT test rig

Table 1. Main geometric dimensions of impeller (PAT mode)

Parameters	Value	Parameters	Value	Parameters	Value	Parameters	Value
Inlet diameter (mm)	260	Blade thickness (mm)	3.4	No. of blades	5	Inlet blade angle (°)	21.7
Outlet diameter (mm)	100	Inlet width (mm)	15.5	Shroud thickness (mm)	5		

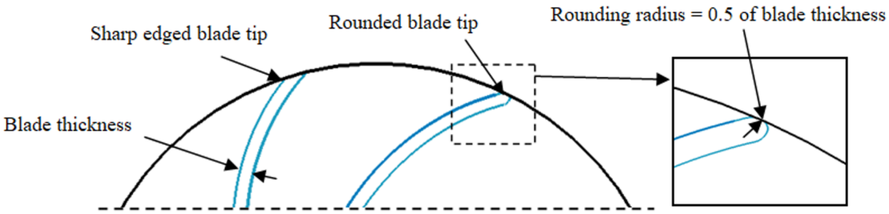

Fig. 2. Impeller blade rounding [12]

3. Numerical methodology

3.1. Computational model of the PAT

The computational model consists of a volute, impeller, front cavity, and back cavity. Usually, as observed in the literature, front and back cavities are not considered to perform the numerical simulation in PAT as well as pump mode operations. But, in the present research, the actual shape and size of the front and back cavities are contemplated, as shown in Fig. 3, to understand the influence of these regions on internal flow physics and the performance of the PAT. For maintaining flow stability through the PAT, the length of the inlet and outlet sections of PAT are extended by four times the respective diameters of the inlet/outlet, as shown in Fig. 3a [13, 23].

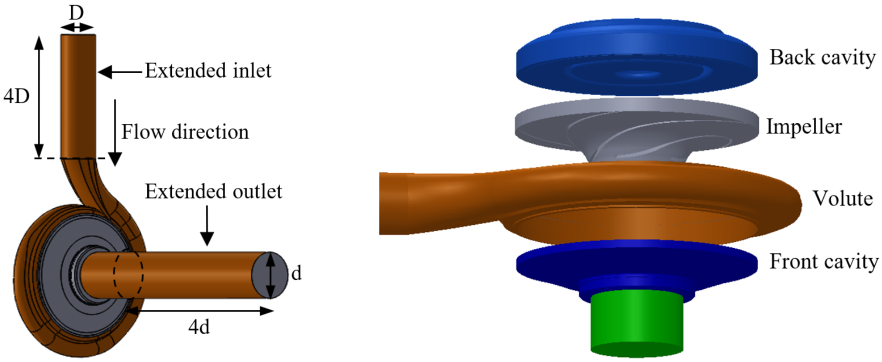

(a) extended inlet and outlet (b) exploded view

Fig. 3. Computational model of PAT

3.2. Mesh generation

For mesh generation, the selection of the element is an important aspect. In this PAT model, an unstructured tetrahedral element is used to mesh the entire complex flow domain. The inflation at the boundaries and refinement at the mesh is provided to accurately capture the boundary layer effects [24]. The grid independence study is performed to select the minimum number of elements. The head and efficiency of PAT are obtained by varying the total number of elements, as presented in Fig. 4, and the deviation in the head and efficiency is found 0.35% and 0.5%, respectively, at the minimum number of elements equal to 3220215. The generated mesh is shown in Fig. 5. The y+ near the boundary wall is 2.

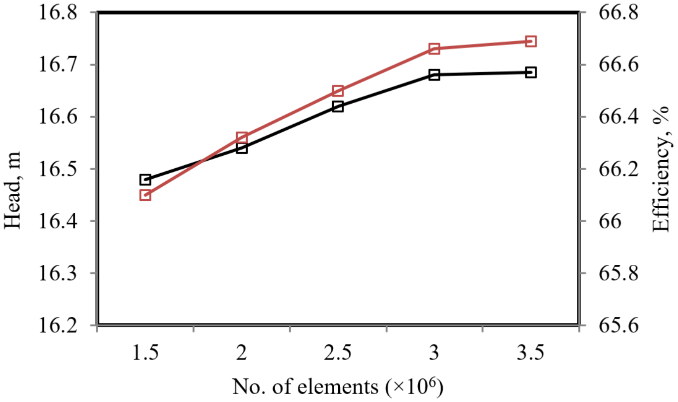

Fig. 4. Grid independence study

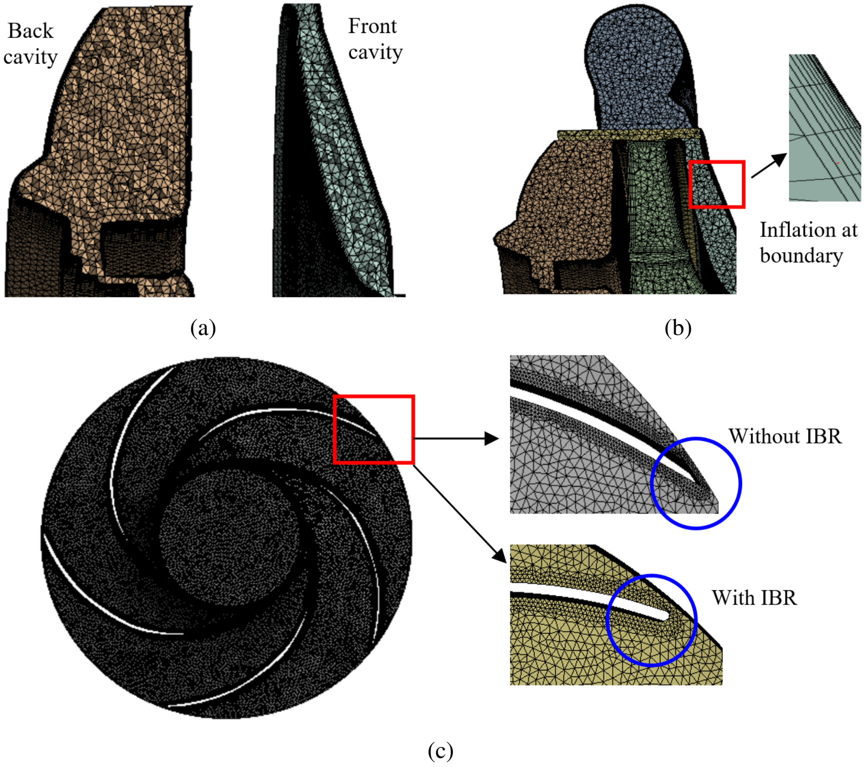

Fig. 5. Mesh of a) cavities b) PAT assembly c) impeller

3.3. Numerical simulation

The CFD code ANSYS-Fluent is used for the numerical simulation. The water is a working fluid with the inlet boundary conditions as pressure inlet and mass flow rate as an outlet. The ε of the volute and impeller are 8.37 µm and 6.37 µm, respectively, measured with the surface roughness tester. Therefore, the ε of the inner surface of the volute, the outer surfaces of the back cavity, and the front cavity (refer Fig. 6) are set to 8.37 µm. The ε of 6.37 µm is set to the impeller blades and the inner and outer shroud surfaces. The k-ω SST turbulence model is used for the numerical simulation [16, 25]. The rotational speed of the impeller is set to 1000 rpm. The same rotational speed is set to the impeller outer shroud surfaces (inner surface of back cavity and front cavity). For the numerical simulations, a steady-state condition is assumed for lower computational time.

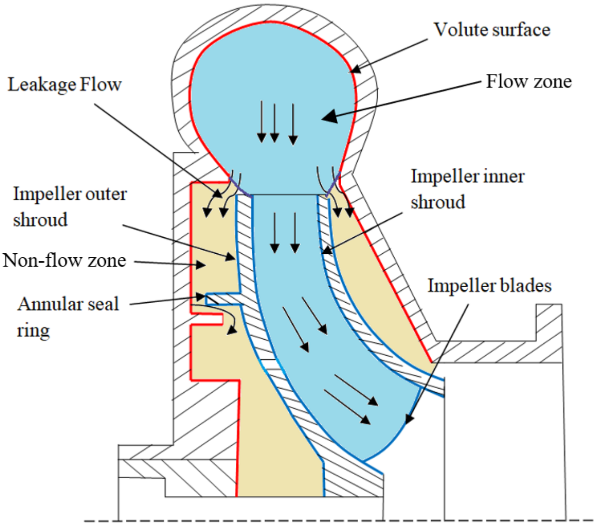

Fig. 6. PAT flow control volume and internal surfaces

4. Results and discussion

In this section, initially in subsection 4.1, the numerical results generated without IBR and with IBR are validated with the experimental results. Afterward, the flow physics at the BEP, part load, and overload conditions are investigated in subsection 4.2 through different plots. Further, in subsection 4.3, the results at different ε at three configurations as listed in Section 1 are presented. The internal flow physics (in the PAT flow zone and non-flow zones), associated hydraulics and disk friction losses, and their influence on the performance parameters are discussed with the help of CFD results in both, subsections 4.2 and 4.3. The detailed evaluation of disk friction losses is presented in Appendix A.3.

4.1. Validation of numerical model

The experimental results generated in Section 2 are compared with results generated by the numerical model for basic PAT characteristics at a constant speed of 1000 rpm and presented in Fig. 7. The numerical results follow almost the

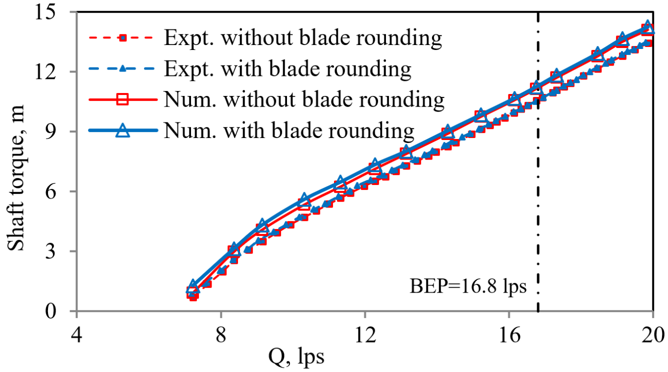

(a) Q vs. shaft torque

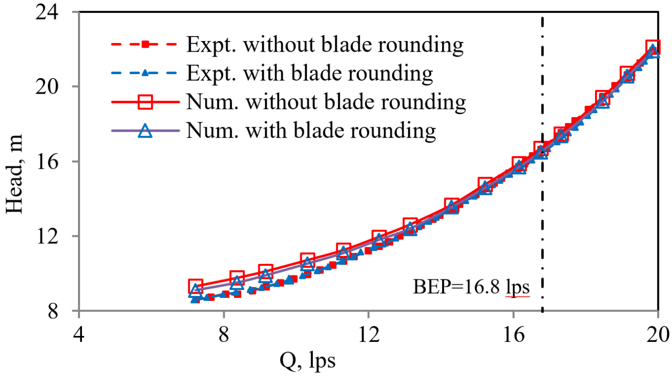

(b) Q vs. head

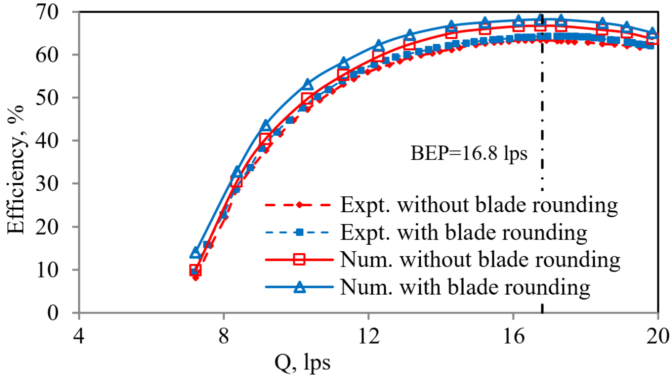

(c) Q vs. efficiency

Fig. 7. Characteristics of PAT with and without IBR by experimentally and numerically

same trend as experimental results for both, without and with IBR stages for the complete range from part load to overload region. Fig. 7a the Shaft torque vs. Flow rate characteristics of experimental and numerical results reflected that the shaft torque curve with the IBR stage is well above that of the without IBR curve for the entire operating range. Further, the numerical shaft torque is consistently greater than experimental shaft torque throughout the entire operating range for without and with IBR. It is observed for head characteristics (see Fig. 7b) that experimental results almost overlap with numerical results of the respective case of without and with IBR. When comparing efficiencies with the IBR stage as shown in Fig. 7c, it is observed that efficiency is over-predicted by numerical analysis due to not considering the mechanical losses in the bearing. As represented in Table 2, the deviation between experimental and numerical results at BEP is less than 7%, which is within the permissible range [26]. The validation of the numerical model developed with experimental results indicates that further numerical analysis will give suitable results and be definitely applicable in practice.

Table 2. Comparative assessment of the PAT performance without IBR and with IBR stage at BEP

	Without IBR			With IBR		
Results	Numerical	Expt.	Error (%)	Numerical	Expt.	Error (%)
Head (m)	16.69	16.62	+0.4	16.5	16.4	+0.7
Shaft Torque (m)	11.14	10.52	+5.89	11.25	10.54	+6.73
Efficiency (%)	66.6	63.3	+5.24	68	64.26	+5.45

4.2. Investigations on internal flow physics of PAT

When the pump is operated in the reverse mode, the change in internal hydraulics is needed to be studied appropriately to understand the possible scope of improvement. At the without IBR stage, the flow from volute strikes on the pressure side of the blade (PSOB) (in PAT mode operation) where it flows in the reverse direction due to its large backward curved vanes, resulting in the secondary flow formation (see Fig. 8a). Further, towards the tip of the impeller blade at the inlet, flow separated due to sharp blade edges, resulting in a large wake formation at the suction side of the blade (SSOB) (see Fig. 8a). The formation of secondary flows on the PSOB is not similar at all blade passages.

As shown in Fig. 8a without IBR case, blade passages in the counter-clockwise direction from the tongue (along the flow direction), for the first blade passage (see marked in Fig. 8a), it is secondary flow with vortex, but at second passage, only secondary flows are observed. For the third blade passage, there is a bigger size vortex than the first and for the remaining blade passages, it is nearly similar. In the case of the SSOB (refer Fig. 8a), again from a tongue in the flow direction, for the first and second blade, a large wake is seen compared to others. From blade passages 3 to 5, the wake is reduced continuously and found the lowest wake at

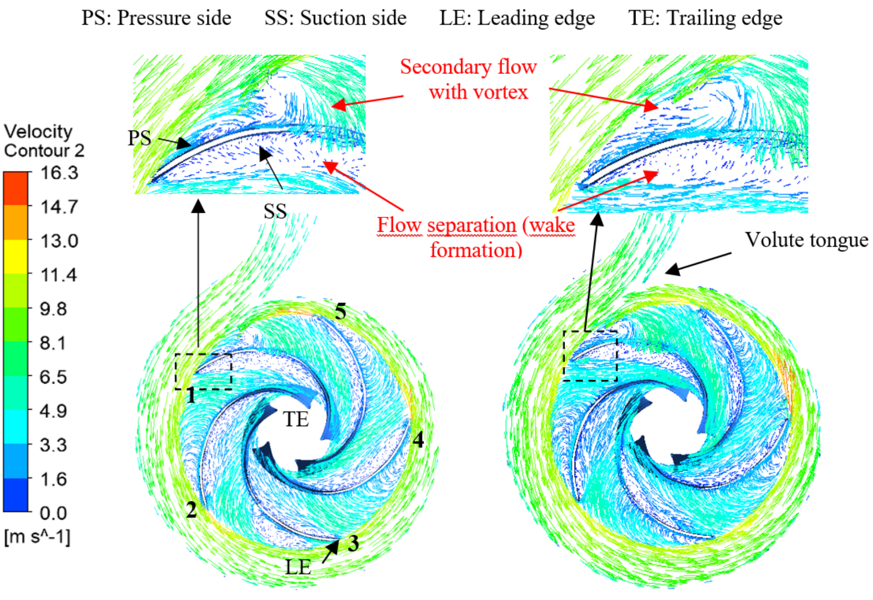

(a) (b)

Fig. 8. Velocity vectors at the mid-span of impeller flow zone at BEP at (a) without IBR and (b) with IBR

the blade passage 5 due to more alignment of flow with the blade angle. Overall, the significant secondary flow on the pressure side and wake on the suction side increase the hydraulic losses and obstruct the flow downstream. While comparing without and with IBR stages, it is observed that secondary flow and wake formations are reduced noticeably, but still, there is a significant scope for further improvement (see Fig. 8 and 9). Furthermore, detailed quantification of separation, secondary flow, and vortex flows in the impeller is required for a better understanding of internal flow physics and its effect on the performance of the PAT.

The determination of the pressure and head based on CFD simulation at various locations (created as stations in CFD) from inlet to outlet is a standard practice followed in pump industries to understand the internal parameters and hence hydraulics for the pumps, which is followed for the PAT. By using it, the total head at different stations, viz. PAT inlet, impeller inlet, impeller outlet, and PAT outlet (all locations in PAT mode) are evaluated for both the stages based on the CFD analysis and presented in Fig. 10, which is helpful to understand subtle changes in the flow physics and the hydraulic losses in the flow-zone. The head from the PAT inlet is initially increased from the PAT inlet to the impeller inlet and then continuously dropped till the PAT exit. The negative head is developed at the PAT outlet as the pump is operated in the reverse mode like a turbine [pressure head is measured with respect to atmospheric pressure head (reference)]. Generally, the PAT outlet is connected with a draft tube wherein the kinetic head is converted

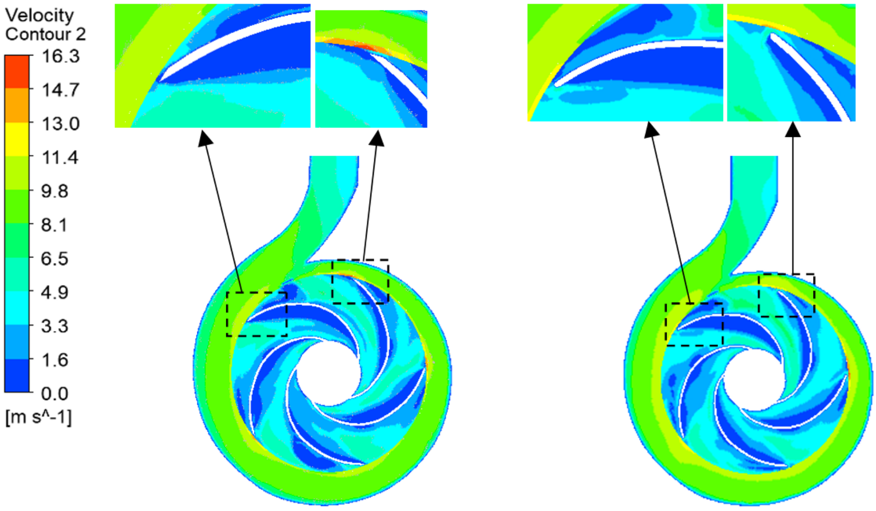

(a) (b)

Fig. 9. Velocity contours at the mid-span of impeller flow zone at BEP at (a) without IBR and (b) with IBR

in the useful pressure head. As shown in Fig. 10, due to IBR modification, the head is decreased from 21.4 m to 21.15 m across the impeller due to reduced wake (hydraulic losses). Additionally, the requirement of the minimal head is dropped from 0.79–0.76 m after IBR modifications. The total heads across the impeller without IBR stage and with IBR stage are 20.61 m and 20.39 m, respectively. The fall in total head across the impeller (0.22 m) due to IBR modifications is nearly equal to the reduction of the head across the PAT (0.19 m), which indicates that the IBR modification is a significant contributor to the decrease in hydraulic losses due to wake, which was also proposed in [5, 6].

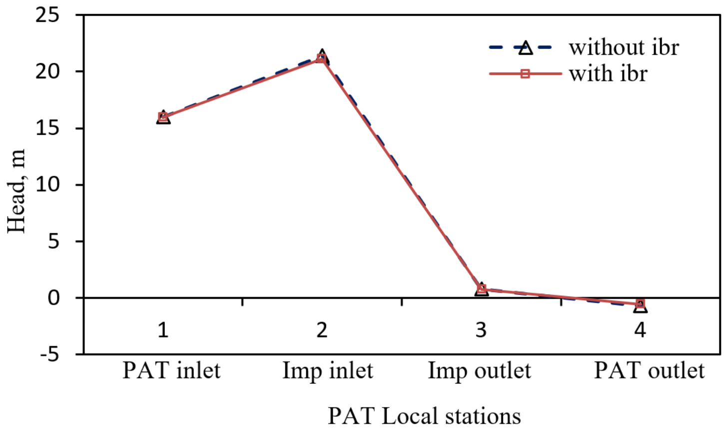

Fig. 10. Head at different stations of PAT at BEP

Fig. 11 generated through the CFD simulation of a PAT is the blade loading plot representing the pressure along the length (from leading to trailing edge) (streamwise 0–1). The five lines at top and bottom each in the graph represent the

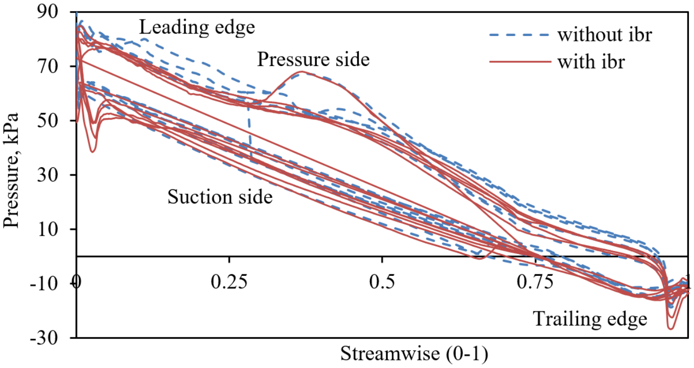

(a) span 0.1

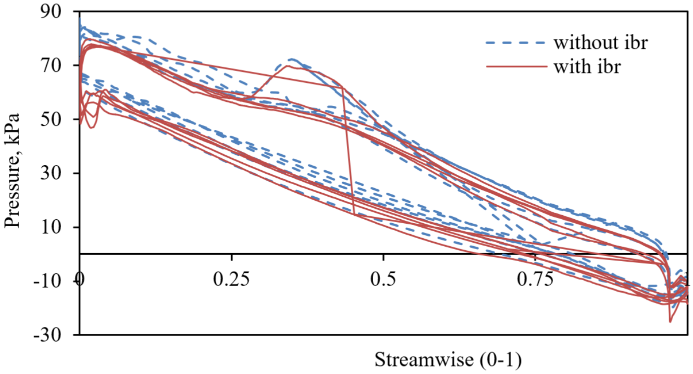

(b) span 0.5

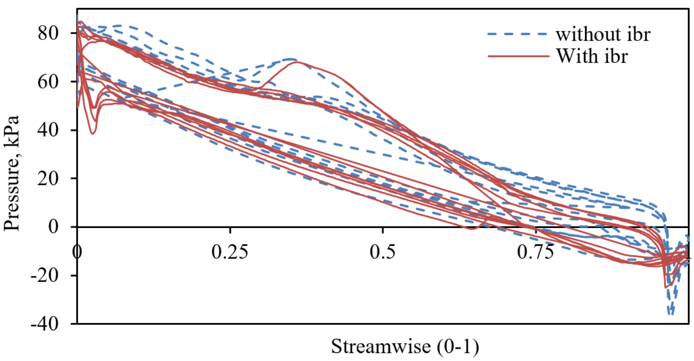

(c) span 0.9

Fig. 11. Blade loading plot at different impeller spans at BEP

pressure at five blades for pressure and suction side of each. The difference between the top and bottom lines represents the pressure difference across the blade profile (pressure and suction sides) from blade inlet to blade exit. It is drawn for various span planes (planes drawn at various distances along the width of impeller) from the front side along the width of the impeller, represented as fractions 0.1, 0.5, and 0.9 of the impeller width. The x-axis represents the blade length along the streamline (0 indicates leading edge, 1 indicates trailing edge). The pressure on both the pressure and suction sides of all the blades at given spans without IBR and with IBR stages from the leading to trailing edge decreases along the flow direction with a lot of fluctuations mainly on the pressure side (see Fig. 11 a–c). For both the pressure and suction sides of all the blades, the pressure lines with the IBR stage are below the pressure lines without the IBR stage, indicating a reduction in the required head due to IBR modifications. The changes in slopes of both pressure lines at the suction and pressure sides indicate there are flow instabilities such as vortex and flow separation, as reported by [16]. Comparatively, at 0.1 and 0.9 spans flow is more complex than at 0.5 spans.

As compared with BEP, for the part-load condition (Q = 8.36 lps), the wake region is significantly large leading to a tiny flow passage. After modifications with IBR, this wake region is reduced not significantly but noticeably as shown in Fig. 12. At blade passage 1, the velocity at the suction side is increased. Similarly, at the blade passage 2–4, velocity is increased specifically at the suction side and wake is reduced. But, the highest increment in the velocity is observed at blade passage 5 as highlighted in Fig. 12b.

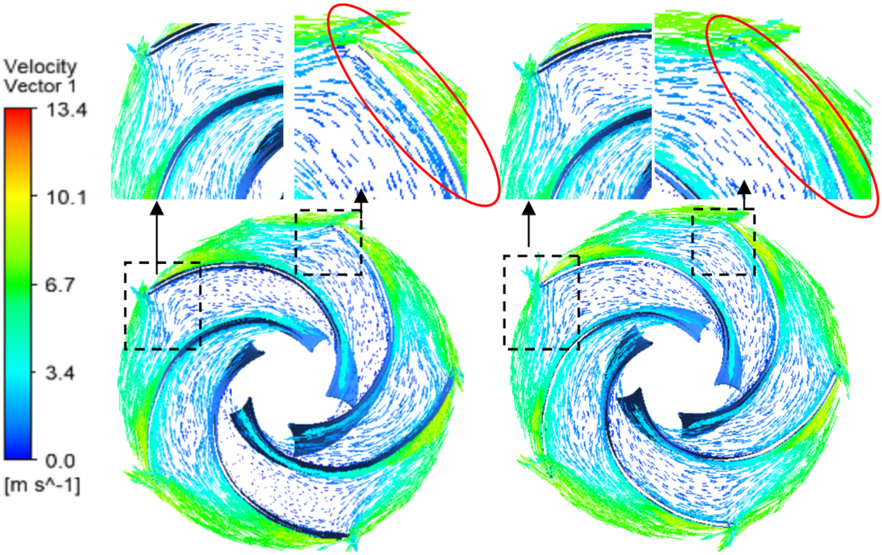

(a) without IBR (b) with IBR

Fig. 12. Velocity vectors at part load condition (Q = 8.36 lps)

At the overload condition (Q = 19.45 lps), the wake region is comparatively larger than at BEP but smaller than that of the part load condition. Similar to the part load condition, the wake region is reduced by a small margin for the overload condition, as shown in Fig. 13. For both the part load and overload conditions, a small increment in efficiency is observed due to a slight reduction of wake at the suction side.

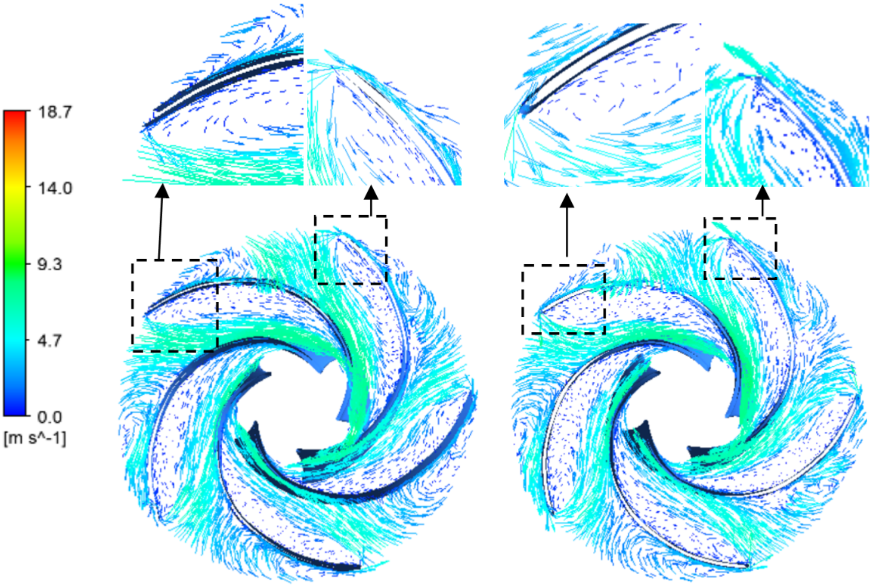

(a) without IBR (b) with IBR

Fig. 13. Velocity vectors at over load condition (Q = 19.45 lps)

4.3. Influence of surface roughness

As discussed in Section 1, due to the continuous operation of PAT in silt water, its ε will change depending on the characteristic parameters of the silt and the material properties of PAT in contact. Generally, from the literature, it is observed that ε will have a value in the range of 0–70 µm. The effect of ε for three different configurations listed in Section 1 is presented in this section.

Configuration i: Uniformly varying the surface roughness

In this section, all components of PAT are subjected to uniform ε, having values as 0 µm, 10 µm, 30 µm, 50 µm, and 70 µm. In order to analyze the cumulative effect of IBR and ε, the results are analyzed for without IBR and with IBR stage at BEP with the help of the flow physics and equations proposed by [6]. As presented in Fig. 14, with an increase in ε from 0–70 µm (in the step of 0, 10, 30, 50, and 70 µm), shaft torque is decreased continuously; with maximum reduction for ε = 70 µm by 1.18 m (10.6%) and 1.15 m (10.2%) for without IBR and with IBR stages, respectively. The decrease in shaft torque indicates that the non-flow zone losses are increased [6]. It can be interpreted as, with the increase of ε, the secondary flow at the front and back cavity is increased, as shown in Fig. 15, causing an increase in secondary flow-based disk friction losses from 0.36 m (at $\varepsilon = 0$ µm) to 0.70 m (at $\varepsilon = 70$ µm). On the other hand, for all surfaces having $\varepsilon = 70$ µm, the head is also decreased significantly by the margin of 0.81 m (5%) and 0.84 m (5.2%) without IBR and with IBR stages, respectively.

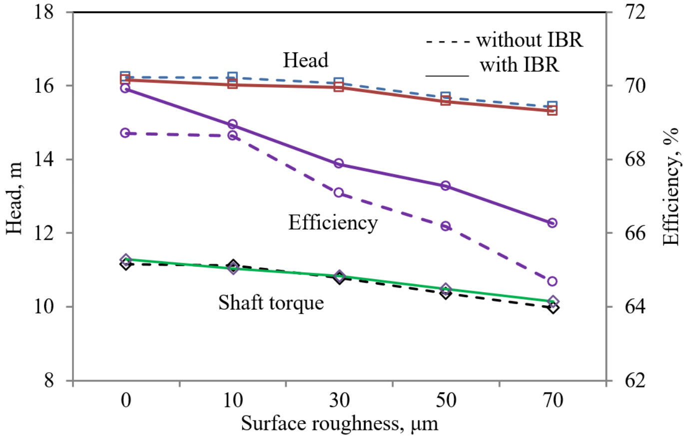

Fig. 14. PAT performance at different surface roughness at BEP for stage *i*

As the ε increases, the secondary flow at the volute flow zone is increased (refer to Fig. 15). Even for a smooth surface ($\varepsilon = 0$ µm), the wake and secondary

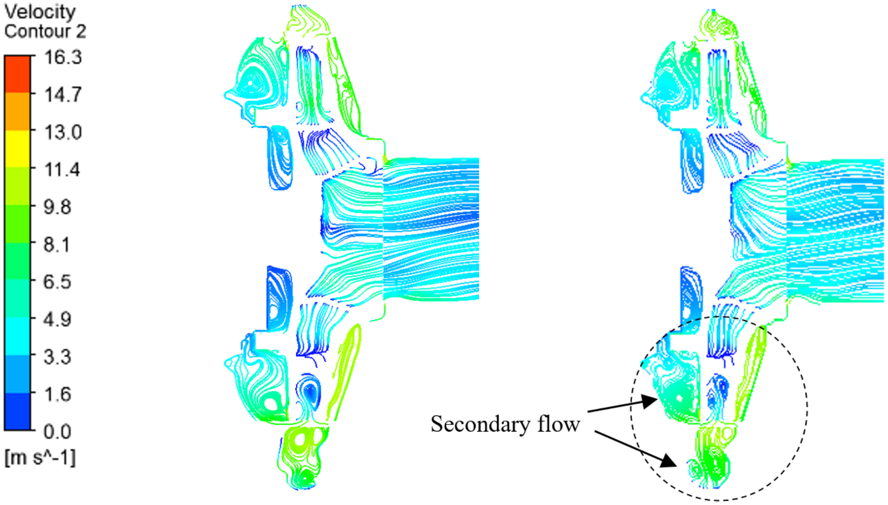

(a) $\varepsilon = 0$ (b) $\varepsilon = 70$ µm

Fig. 15. Meridional plane streamlines at uniformly varying ε (without IBR)

flow are formed on the SSOB and PSOB, respectively, for both the stages, as discussed in Subsection 4.1. But, with the increase of ε, the wake and secondary flow at the impeller flow zone are further increased, as depicted in Fig. 16. Overall, with an increase in ε, there is mainly an increase in secondary flow-based disk friction losses at the non-flow zone by a significant margin. While, contributions of the hydraulic losses at the volute and flow zone control volume is less in the deterioration of PAT performance. Because of above mentioned two effects, the efficiency reduction in the PAT is noticed by 4% and 3.7% (absolute) for the without IBR and with IBR stages, respectively. The ε of impeller blades does not have much effect on the rise in respective losses mainly on the suction side because of flow separation.

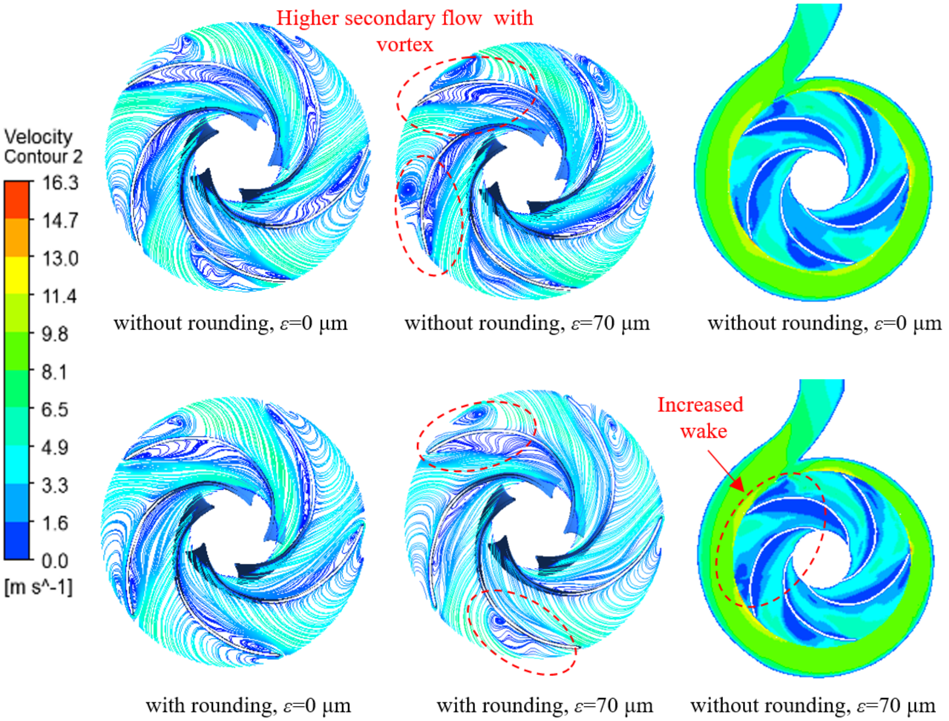

Fig. 16. Streamlines and velocity contours at uniformly varying surface roughness

Configuration ii: Varying the surface roughness at volute and constant at the impeller without IBR

The impeller manufactured by the casting process can be smoothened effectively by the machining process. But, it is challenging to machine the inner surface of the volute. Therefore, the PAT commonly operated with a smooth impeller in the relatively rough volute. This section analyzes the influence of volute ε on the

PAT performance at BEP without the IBR stage. The numerical simulations are performed by changing the volute's internal ε (0, 10, 30, 50, and 70 µm), keeping the surface roughness of the impeller constant (0 µm). The results are presented in Fig. 17.

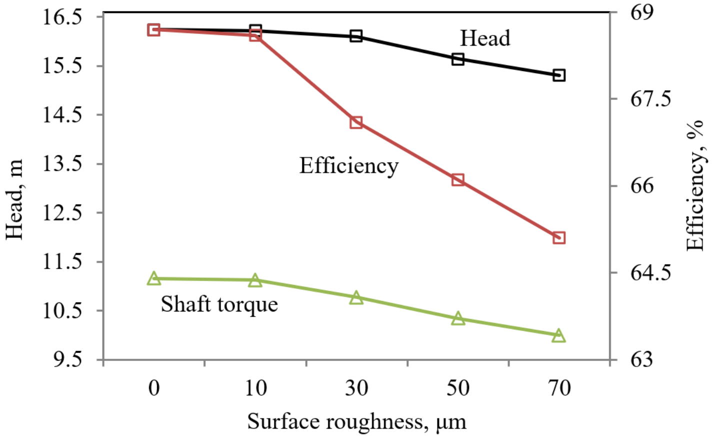

Fig. 17. PAT performance at different ε of volute at BEP

As ε increases from 0–70 µm, the shaft torque decreases by 1.2 m (10.4%), while the head of the PAT decreases by 0.95 m (5.8%). The significant reduction of shaft torque indicates that the non-flow zone losses are increased [6]. As depicted in Fig. 18 (a–b), the secondary flow at the back cavity increased with the increase of volutes ε, which is also reported by authors [27]. But the disk friction loss evaluated from equation (A4) is under-predicted. Further, secondary flow is increased at the volute with an increase of ε (refer Fig. 18 a–b). The greater reduction of shaft torque

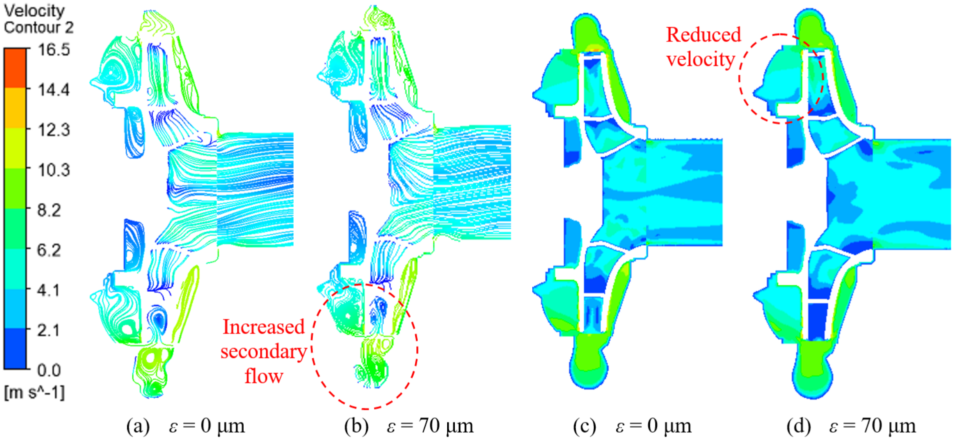

(a) $\varepsilon = 0$ µm (b) $\varepsilon = 70$ µm (c) $\varepsilon = 0$ µm (d) $\varepsilon = 70$ µm

Fig. 18. Streamlines and velocity contours at meridional plane at different ε of volute

than head and minimal increment in the disk friction losses (non-flow zone losses) indicate a substantial rise in the flow zone losses. As the ε of volutes increases, the velocity at the back cavity decreases, as presented in Fig. 18 (c–d). Further, as shown in Fig. 19 and 20, the velocity and pressure are dropped at the near wall boundary of the volute due to an increase in the friction between the volutes solid wall and fluid layer.

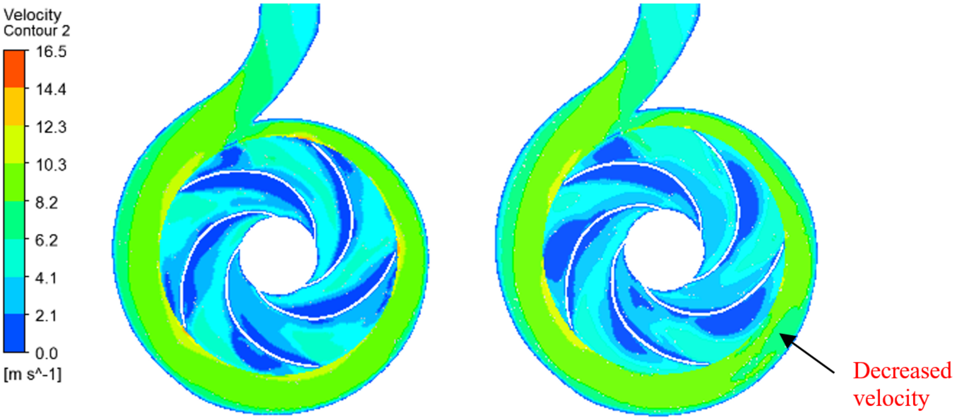

(a) $\varepsilon = 0$ µm (b) $\varepsilon = 70$ µm

Fig. 19. Velocity contours at different volutes surface roughness

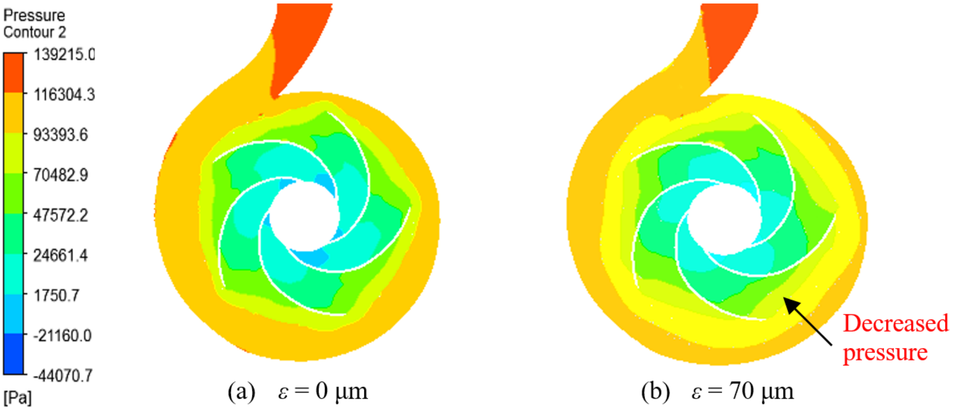

(a) $\varepsilon = 0$ µm (b) $\varepsilon = 70$ µm

Fig. 20. Pressure contours at different volutes surface roughness

Surprisingly, the ε of the volute changed the internal flow physics of the impeller flow zone due to a change in hydraulics between the volute tongue and impeller inlet. The wake formed at the blade suction side increases with the increase in volutes ε, as shown in Fig. 19b. Due to the cumulative effect of increased secondary flow and friction at the volute flow passage, secondary flow at the back cavity, and increased wake in the impeller flow zone, the PAT efficiency deteriorates by 3.6% (absolute).

Configuration iii: Varying the surface roughness at the impeller and constant at volute

The numerical simulations are performed by changing the ε of the impeller blades and inner and outer shroud surfaces within the range of 0 to 70 µm. The ε of the volute surface and fixed surfaces of cavities are kept constant (ε = 0 µm). The performance of PAT at different ε of the impeller at BEP is represented in Fig. 21. A small increment in the shaft torque is observed at the ε of 10 µm. On the other hand, the head is also increased. PAT's output power is increased at the expense of increased input power consumption, as the author [28] reported in pump mode. But, as the ε is increased from 10 µm to 70 µm, the shaft torque and head both decreased. The shaft torque is reduced from 11.16 m to 10.7 m (3.8%) with a slight head drop. The percentage of shaft torque is reduced more than the head, resulting decrease in PAT's efficiency from 68.7% to 66.2% (2.5% absolute). The reduction of shaft torque indicates an increase in non-flow zone losses. It is approved by the change in the flow physics of the non-flow zone. The secondary flow at the back and front cavity is increased with the impeller's outer shroud ε, as shown in Fig. 22. Hence, the disk friction loss is increased by 0.27 m. In addition, wake is also increased at the blade suction side, as shown in Fig. 23, due to the higher ε of the impeller blade. Therefore, increased secondary flow at the non-flow zone and wake at the blade suction side are responsible for the deterioration of the PAT's efficiency.

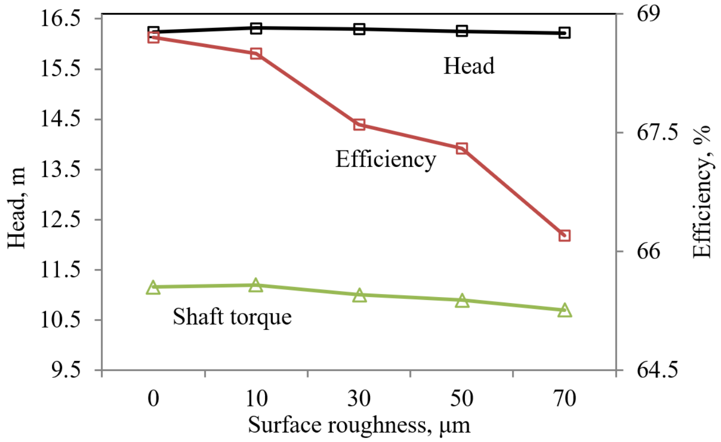

Fig. 21. PAT performance at different ε of impeller at BEP

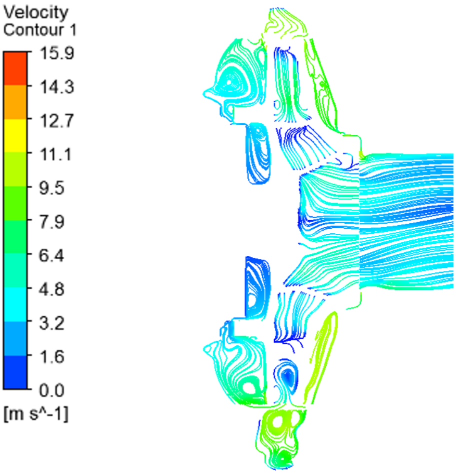

(a) $\varepsilon = 0$ µm (b) $\varepsilon = 70$ µm

Fig. 22. Meridional plane streamlines at different surface roughness of impeller

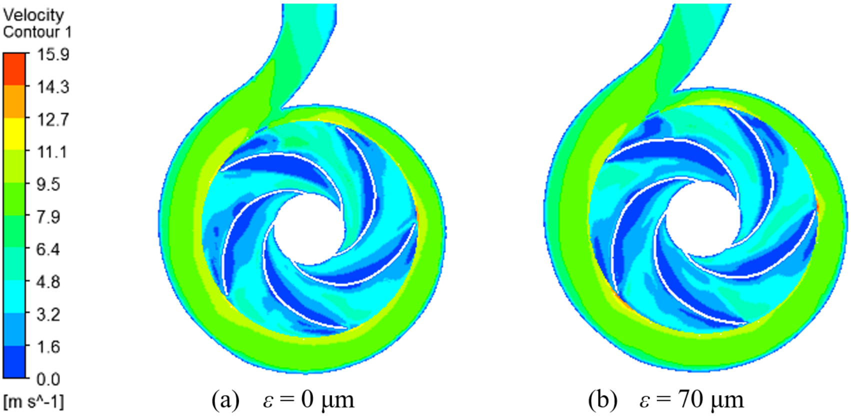

(a) $\varepsilon = 0$ µm (b) $\varepsilon = 70$ µm

Fig. 23. Velocity contours at impeller midplane at different ε of the impeller

Summary on the influence of surface roughness

For all the configurations, as the ε is increased, the head and shaft torque of the PAT is decreased. The maximum reduction of the head is 5.8% for configuration ii. While the maximum shaft torque is reduced by 10.6% for configuration i. The net reduction of shaft torque than reduction of head deteriorated the PAT efficiency for all the configurations. The maximum drop in the efficiency is 4% (absolute) for configuration i, without the IBR stage due to increased secondary flow-based disk friction losses, increased secondary flow at the blade pressure side. For configuration ii, the secondary flow at the volute flow zone and friction between fluid and volute internal surface and wake at the blade suction side decreased the efficiency. While for configuration iii, secondary flow-based disk friction losses and wake at the blade suction side contribute to the efficiency drop.

5. Conclusions

A CFD-based numerical investigation is performed to analyze the internal hydraulics and the performance of PAT due to the impeller blade rounding and rise in surface roughness of the volute and impeller. The agreement of numerical and experimental results showed that the quality of the mesh and turbulence model selected for the numerical simulation was appropriate and simulation results are close to the physical situation. The investigation revealed the following meaningful conclusions:

1. Modification of the impeller blade rounding reduced the losses at the entry of the impeller and subsequently the wake at the blade suction side by a small margin, increasing the efficiency of PAT up to 1.4% for the selected PAT of low specific speed. It is important to note that after blade rounding, there are still significant hydraulic losses observed in numerical solution due to wake formation on the suction side of the blades indicating that radical modifications, such as an appropriate change in the blade profile or on the blade suction side and/or pressure side to reduce the wake, will definitely improve the efficiency significantly.
2. Similar to a centrifugal pump, surface roughness is one of the critical parameters affecting the efficiency of PAT. It is important to note that the increase in surface roughness, the torque, head, and efficiency of PAT decrease due to adverse changes in the internal flow hydraulics at the flow zone by a small margin and at the non-flow zone by a significant margin.
3. With the rise of volutes surface roughness from 0 µm to 70 µm, efficiency reduces by 3.6% due to the increase of the secondary flow and friction at the volute flow zone and the wake at the blade suction side. With the increase of impellers' outer shroud surface roughness (0 to 70 µm), the secondary flow-based disk friction losses at the non-flow zone are increased. Furthermore, wake is also increased at the blade suction side cumulatively resulting in the reduction of the PAT efficiency by 2.5%. The maximum decrease in efficiency is 4% when the surface roughness of both, the volute and impeller, are increased uniformly from 0 µm to 70 µm.
4. Overall, the investigation revealed that the surface roughness of the volute is a significant contributor to reducing the PAT efficiency. The efficiency of PAT can be increased by simple modifications like polishing the rough inner surface of the volute.

This work can extend to quantify the flow irreversibility noticed in the impeller and also indicates flow separation points with vortex by numerical means. There is scope to improve the performance of PAT by implementing suitable modifications to reduce the proposed losses such as separation by multi-material welding approach for filling of material of appropriate size and shape combination on the blade suction/pressure side.

A. Appendix

A.1. Test rig instrumentation

The instrument details and accuracy is listed in Table A1. The absolute and relative uncertainties in the measurement are illustrated in Table A2. The absolute uncertainty in the efficiency is ±0.36 and ±0.37 for without IBR and with IBR stage, respectively. While relative uncertainty for both stages is ±0.57. As shown in Fig. A1, two sets of readings have been taken to ensure the repeatability. The head, shaft torque, and efficiency for both sets show an almost overlapping trend.

Table A1. Summary of instruments and accuracy

Instruments	Parameters	Make	Range	Accuracy
Pressure transmitter	Inlet Pressure	Honeywell	0 to 3.5 bar	±0.065% of the span
	Outlet Pressure	Honeywell	0 to –1 bar	±0.065% of the span
Flow transmitter	Flow rate	E &H	0 to 50 lps	±0.5% of full scale reading
Torque sensor	Torque	Honeywell	0 to 50 Nm	±0.05% of full scale reading
Speed sensor	Speed	–	0 to 3000 rpm	±1 rpm

Table A2. Summary of uncertainty in the measurement

Parameters		Without IBR	With IBR
Speed	ΔN (rpm)	±1	–
	$\Delta N/N$ (%)	±0.1	–
Discharge	Q (lps)	16.73	16.73
	ΔQ (lps)	±0.08	–
	$\Delta Q/Q$ (%)	±0.5	–
Head	H (m)	16.62	16.39
	ΔH (m)	±0.03	±0.03
	$\Delta H/H$ (m)	±0.21	±0.22
Torque	T (N-m)	16.49	16.52
	ΔT (N-m)	±0.025	±0.025
	$\Delta T/T$ (N-m)	±0.15	±0.15
Efficiency	η	63.38	64.26
	$\Delta\eta$	±0.36	±0.37
	$\Delta\eta/\eta$	±0.57	±0.57

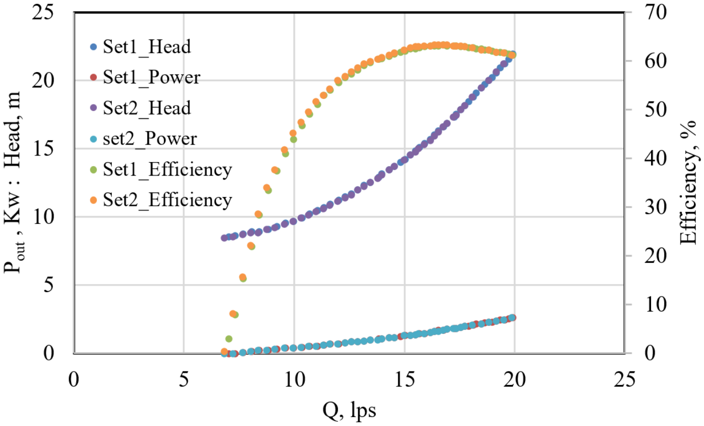

Fig. A1. Repeatability of measuring the PAT performance parameters

A.2. Impeller sections and diameters

Fig. A2 represents the computational model of impeller showing inlet and outlet diameters.

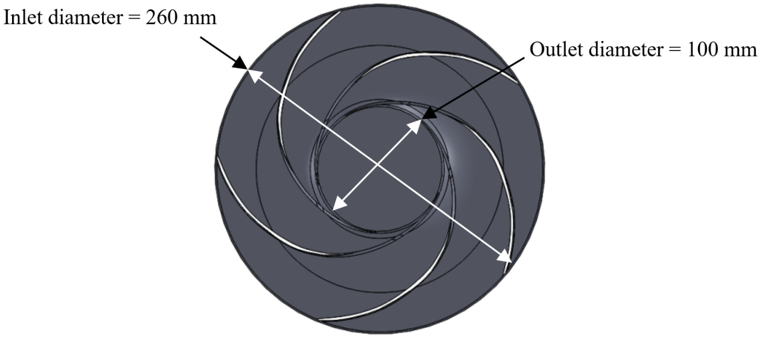

Fig. A2. Impeller inlet and outlet specification

A.3. Disk friction calculations

In this section, disk friction losses are calculated based on the theoretical model proposed by the author [29]. Table A3 represents the dimensions of various geometric parameters of the back cavity and impeller. The rotation factor, friction factor, disk friction factor and power consumption per side of the disk are evaluated from Eq. (A1), (A2), (A3) and Eq. (A4), respectively.

$$k_0 = \frac{1}{1 + \left(\frac{r_w}{r_2}\right)^2 \sqrt{\left(\frac{r_w}{r_2} + 5\frac{t_{ax}}{r_2}\right) \frac{c_{f,\text{volute}}}{c_{f,\text{impeller}}}}}, \tag{A1}$$

$$C_f = \frac{0.136}{\left\{-\log\left(0.2\frac{\varepsilon}{r_2} + \frac{12.5}{\mathrm{Re}}\right)\right\}^{2.15}}, \tag{A2}$$

$$k_{RR} = \frac{\pi}{2\mathrm{Re}S_{ax}} + \frac{0.0625}{\mathrm{Re}^{0.2}}.(1-k_0)^{1.75}\, f_{R,\mathrm{imp}} f_L\,, \tag{A3}$$

$$P_{RR} = \frac{k_{RR}}{\cos\delta}\rho\omega^3 r_2^5\left\{1-\left(\frac{r_1}{r_2}\right)^5\right\}, \tag{A4}$$

where δ is the angle made by the impeller outer shroud with an axis perpendicular to the shaft axis of the PAT. Fig. A3 shows the terminology of back cavity and impeller parameters used in the equations. Detailed evaluation of disk friction losses at configuration i of PAT is illustrated in Table A4. Similarly, disk friction losses for configurations ii and iii can be evaluated.

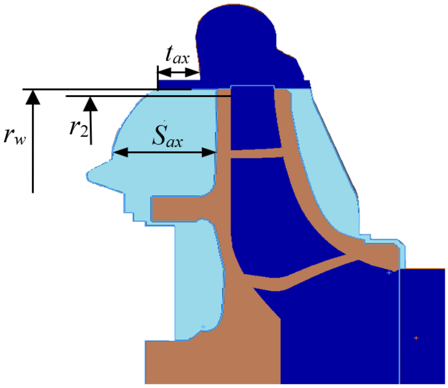

Fig. A3. Geometric parameters of back cavity and impeller

Table A3. Back cavity and impeller dimensions

Parameters	Dimensions (mm)	Parameters	Dimensions (mm)	Parameters	Dimensions (°)
t_{ax}	14.75	r_w	133	δ	0
S_{ax}	33.5	r_2	130		

Table A4. Evaluation of the disk friction losses at different ε (Re = 1764470)

Configurations	$\varepsilon_{\mathrm{imp}}$ (µm)	$\varepsilon_{\mathrm{vol}}$ (µm)	C_f, vol	C_f, imp	k_0	P_{RR}, (W)	Disk friction loss (m)
i	0	0	0.00355	0.00355	0.397	58.847	0.36
	10	10	0.00483	0.00483	0.397	79.651	0.48
	30	30	0.00590	0.00590	0.397	97.007	0.59
	50	50	0.00657	0.00657	0.397	107.847	0.65
	70	70	0.00708	0.00708	0.397	116.170	0.70

References

[1] P.P. Sharma, S. Chatterji, and B. Singh. Techno-economic analysis and modelling of standalone versus grid-connected small hydropower systems – a review of literature. *International Journal of Sustainable Energy*, 32(1):1–17, 2013. doi: 10.1080/14786451.2011.591492.

[2] S. Mishra, S.K. Singal and, D.K. Khatod. Cost analysis for electromechanical equipment in small hydropower projects. *International Journal of Green Energy*, 10(8):835–847, 2013. doi: 10.1080/15435075.2012.727367.

[3] M. Binama, W.T. Su, X.B. Li, F.C. Li, X.Z. Wei, and S. An. Investigation on pump as turbine (PAT) technical aspects for micro hydropower schemes: A state-of-the-art review. *Renewable and Sustainable Energy Reviews*, 79:148–179, 2017. doi: org/10.1016/j.rser.2017.04.071.

[4] M.H. Shojaeefard and S. Saremian. Effects of impeller geometry modification on performance of pump as turbine in the urban water distribution network. *Energy*, 255:124550, 2022. doi: 10.1016/j.energy.2022.124550.

[5] P. Singh. *Optimization of internal hydraulics and of system design for pumps as turbines with field implementation and evaluation*. Ph.D. Thesis, Karlsruhe University, Germany, 2005.

[6] A. Doshi, S. Channiwala, and P. Singh. Inlet impeller rounding in pumps as turbines: An experimental study to investigate the relative effects of blade and shroud rounding. *Experimental Thermal and Fluid Science*, 82:333–348, 2017. doi: 10.1016/j.expthermflusci.2016.11.024.

[7] M.A. Ismail and H. Zen. CFD modelling of a pump as turbine (PAT) with rounded leading edge impellers for micro hydro systems. *Proc. MATEC Web of Conferences*, 87:05004, 2017. doi: 10.1051/matecconf/20178705004.

[8] M. Suarda, N. Suarnadwipa, and W.B. Adnyana. Experimental work on modification of impeller tips of a centrifugal pump as a turbine. *Proc. The 2nd Joint International Conference on Sustainable Energy and Environment (SEE 2006)*, pages 21–25, Bangkok, Thailand, 2006.

[9] H. Yang, L. Zhu, H. Xue, J. Duan, and F. Deng. A numerical analysis of the effect of impeller rounding on centrifugal pump as turbine. *Processes*, 9(9):1673, 2021. doi: 10.3390/pr9091673.

[10] A. Doshi, S. Channiwala, and P. Singh. Influence of nonflow zone (back cavity) geometry on the performance of pumps as turbines. *Journal of Fluids Engineering*, 140(12):121107, 2018. doi: 10.1115/1.4040300.

[11] S.-S. Yang, F.Y. Kong, J.-H. Fu, and L. Xue. Numerical research on effects of splitter blades to the influence of pump as turbine. *International Journal of Rotating Machinery*, 2012:123093. doi: 10.1155/2012/123093.

[12] A. Doshi. *Influence of impeller inlet rounding and shape of non-flow zones on the performance of pump as turbine*. Ph.D. Thesis, Sardar Vallabhbhai National Institute of Technology, Surat, India, 2016.

[13] S. Derakhshan and N Kasaeian. Optimization, numerical, and experimental study of a propeller pump as turbine. *Journal of Energy Resources Technology*, 136(1):012005, 2014. doi: 10.1115/1.4026312.

[14] S-.S. Yang, H.-L. Liu, F.-Y. Kong, B. Xia, and L.-W. Tan. Effects of the radial gap between impeller tips and volute tongue influencing the performance and pressure pulsations of pump as turbine. *Journal of Fluids Engineering*, 136(5):054501, 2014. doi: 10.1115/1.4026544.

[15] S.-C. Miao, J.-H. Yang, G.-T. Shi, and T.-T. Wang. Blade profile optimization of pump as turbine. *Advances in Mechanical Engineering*, 7(9), 2015. doi: 10.1177/1687814015605748.

[16] T. Lin, Z. Zhu, X. Li, J. Li, and Y. Lin. Theoretical, experimental, and numerical methods to predict the best efficiency point of centrifugal pump as turbine. *Renewable Energy*, 168:31–44, 2021. doi: 10.1016/j.renene.2020.12.040.

[17] D.L. Zariatin, D. Rahmalina, E. Prasetyo, A. Suwandi, and M. Sumardi. The effect of surface roughness of the impeller to the performance of pump as turbine pico power plant. *Journal of Mechanical Engineering and Sciences*, 13(1):4693–4703, 2019. doi: 10.15282/jmes.13.1.2019.24.0394.

[18] L. Zemanová and P. Rudolf. Flow inside the sidewall gaps of hydraulic machines: a review. *Energies*, 13(24):6617, 2020. doi: 10.3390/en13246617.

[19] S. Sangal, M.K. Singhal, and R.P. Saini. Hydro-abrasive erosion in hydro turbines: a review. *International Journal of Green Energy*, 15(4):232–253, 2018. doi: 10.1080/15435075.2018.1431546.

[20] J.F. Santa, J.C. Baena, and A. Toro. Slurry erosion of thermal spray coatings and stainless steels for hydraulic machinery. *Wear*, 263(1-6):258–264, 2007. doi: 10.1016/j.wear.2006.12.061.

[21] M. Singh, J. Banerjee, P.L. Patel, and H. Tiwari. Effect of silt erosion on Francis turbine: a case study of Maneri Bhali Stage-II, Uttarakhand, India. *ISH Journal of Hydraulic Engineering*, 19(1):1–10, 2013. doi: 10.1080/09715010.2012.738507.

[22] M. Sharma, D.K. Goyal, and G Kaushal. Tribological investigation of HVOF sprayed coated turbine steel under varied operating conditions. *Materials Today: Proceedings*, 24(2):869–879, 2020. doi: 10.1016/j.matpr.2020.04.397.

[23] T. Asim and R. Mishra. Large-Eddy-Simulation-based analysis of complex flow structures within the volute of a vaneless centrifugal pump. *Sādhanā*, 42(4):505–516, 2017. doi: 10.1007/s12046-017-0623-y.

[24] R. Gupta and A. Biswas. CFD analysis of flow physics and aerodynamic performance of a combined three-bucket Savonius and three-bladed Darrieus turbine. *International Journal of Green Energy*, 8(2):209–233, 2011. doi: 10.1080/15435075.2010.548541.

[25] K. Rogowski, R. Maroński, and J. Piechna. Numerical analysis of a small-size vertical-axis wind turbine performance and averaged flow parameters around the rotor. *Archive of Mechanical Engineering*, 64(2):205–218, 2017. doi: 10.1515/meceng-2017-0013.

[26] J. Gülich. *Centrifugal Pump.*: Springer, Berlin, 2008.

[27] G. Varghese, T.M. Kumar, and Y.V.N. Rao. Influence of volute surface roughness on the performance of a centrifugal pump. *Journal of Fluids Engineering*, 100(4):473–476, 1978. doi: 10.1115/1.3448710.

[28] F.A. Varley. Effects of impeller design and surface roughness on the performance of centrifugal pumps. *Proceedings of the Institution of Mechanical Engineers*, 175(1):955–989, 1961. doi: 10.1243/PIME_PROC_1961_175_062_02.

[29] J.F. Gülich. Disk friction losses of closed turbomachine impellers. *Forschung im Ingenieurwesen*, 68(2):87–95, 2003. doi: 10.1007/s10010-003-0111-x.